Embedded Ni nanoparticles in CeZrO2 as stable catalyst for dry reforming of methane

André L.A. Marinho, Raimundo C. Rabelo-Neto, Florence Epron, Nicolas Bion, Fabio S. Toniolo, Fabio Bellot Noronha

HAL Id: hal-02903461
https://hal.archives-ouvertes.fr/hal-02903461

Submitted on 27 Nov 2020

Embedded Ni nanoparticles in CeZrO₂ as stable catalyst

for dry reforming of methane

André L. A. Marinho [1,2,3], Raimundo C. Rabelo-Neto[2], Florence Epron [3], Nicolas Bion [3], Fabio S. Toniolo [1], Fabio B. Noronha[2,*]

[1] Federal University of Rio de Janeiro, Chemical Engineering Program of COPPE/UFRJ, P.O. Box 68502, CEP 21941-972, Rio de Janeiro, RJ, Brazil.

[2] National Institute of Technology, Catalysis Division, Rio de Janeiro, RJ 20081-312, Brazil.

[3] University of Poitiers, Institut de Chimie des Milieux et Matériaux de Poitiers (IC2MP), TSA51106 – F86073 Poitiers Cedex 9, France

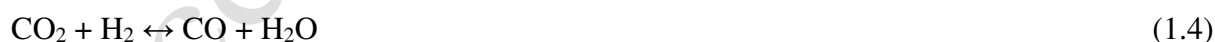* Corresponding author: fabio.bellot@int.gov.br

1

Abstract

Ni nanoparticles embedded in CeO_2 (Ni@CeO_2) and $CeZrO_2$ (Ni@$CeZrO_2$) were synthesized by sol-gel method and compared with a Ni/CeO_2 prepared by support impregnation. The performance of the catalysts was investigated for dry reforming of methane reaction. In situ XRD, XANES and TEM showed that Ni embedded in CeO_2 improved the resistance to sintering along the reduction at 800ºC. Doping ceria with zirconia inhibited the growth of Ni particles and increased the oxygen mobility. SEM, TEM, Raman spectroscopy and TGA of the used catalysts after dry reforming of methane showed that carbon formation rate was significantly reduced for the catalysts containing Ni nanoparticles embedded in ceria structure. Carbon deposits were not detected over Ni@$CeZrO_2$ after 24 h of reaction. Therefore, the control of Ni particle size and the high oxygen mobility of Ni@$CeZrO_2$ catalyst inhibited carbon deposition and favored the mechanism of carbon removal, promoting catalyst stability.

Key words: Ni-embedded; Ceria; Ceria-Zirconia; Oxygen Isotopic Exchange; Methane Dry Reforming; Biogas.

1- Introduction

Biogas obtained by anaerobic digestion of biomass is a source of CH_4 and CO_2 and it can be regarded as an alternative renewable source of methane. Nowadays, the biogas produced from biomass waste in the farms is mostly used to produce thermal or electrical energy. However, biogas can be used for the production of renewable energy and added-value chemicals [1]. Hydrogen produced via biogas reforming might be used for energy generation on low-temperature fuel cells or it can be directly fed to high-temperature fuel cells [2-5].

Steam reforming of methane is the main industrial process to produce H_2. However, the dry reforming of methane (DRM) (Eq. 1.1), using directly the biogas as feedstock, could be an alternative for obtaining hydrogen [6]. The main limitation of DRM technology is catalyst deactivation due to carbon deposition, which occurs under reaction conditions. DRM is an endothermic reaction ($\Delta H° = 247$ kJ/mol) and requires high reaction temperature, which favors several side reactions, especially CH_4 decomposition (Eq. 1.2), Boudouard reaction (Eq. 1.3) and reverse water-gas shift (RWGS) (Eq. 1.4) [7].

$$CH_4 + CO_2 \leftrightarrow 2\ CO + 2H_2 \tag{1.1}$$

$$CH_4 \leftrightarrow C + 2H_2 \tag{1.2}$$

$$2\ CO \leftrightarrow C + CO_2 \tag{1.3}$$

$$CO_2 + H_2 \leftrightarrow CO + H_2O \tag{1.4}$$

The development of catalysts resistant to deactivation by carbon deposition has been the focus of several studies. Supported metal catalysts have been extensively investigated for the DRM [8,9]. Ni-based catalysts have high activity and low cost, but metal sintering may occur during the DRM and thus favor the production of coke on its surface, leading to catalyst deactivation [10].

3

The high temperature required to perform the DRM favors the metal sintering process, which motivates the development of novel catalysts able to resist to deactivation. Recently, the literature reported a series of catalysts in which the metal phase is embedded into an oxide, improving the catalyst stability by avoiding the metal sintering [11–14]. Ni@SiO$_2$ [15] and Ni@Al$_2$O$_3$ [16] catalysts exhibited high resistance to metal sintering during the DRM but carbon formation was not totally inhibited. The development of metallic Ni particles embedded into oxides with high OSC could combine two advantages: to limit the metal sintering and prevent or remove carbon deposition.

The use of supports with redox properties is reported to improve catalyst stability for the DRM, due to the enhancement of the rate of carbon gasification on the catalyst surface. The use of CeO$_2$ has been investigated as a support in many reactions, which required high oxygen storage capacity (OSC) [17,18]. As a support for the DRM, ceria participates in the dissociative adsorption of CO$_2$ and donates an oxygen atom to the metallic particle containing carbon deposits, promoting the carbon removal mechanism [18]. Furthermore, doping ceria structure with appropriate cations can modify the lattice parameters, increasing the amount of oxygen exchangeable species. The literature reports ZrO$_2$ as an excellent dopant to increase the redox properties of ceria [19–22].

The use of ceria to confine metals has been also investigated [11,23], but the synthesis procedures are quite complex and hardly reproducible with high cost. Recently, Wang et al.[24] synthetized Cu nanoparticles embedded in CeO$_2$ by a simple sol-gel method. The catalysts were tested for hydrogenation of methyl acetate reaction at 400 °C and no sintering was observed. However, to the best of our knowledge, there is still no report in the literature about this sol-gel method for the synthesis of Ni@CeO$_2$ catalyst and its application for the DRM.

In this work, we aim to prepare Ni-embedded CeO$_2$ catalysts using a one-step synthesis method and test them for the DRM. The use of ZrO$_2$ as dopant was also evaluated. A Ni/CeO$_2$

4

catalyst prepared by traditional impregnation method was also tested for comparison. Important structure properties were investigated by Transmission Electron Microscopy, Raman Spectroscopy, in-situ X-ray Diffraction and in-situ X-ray Absorption. The mobility of oxygen in the material was characterized by Oxygen Isotopic Exchange. The carbon formation was analyzed by Thermogravimetric analysis, Raman Spectroscopy, Scanning and Transmission Electron Microscopy.

2.   Experimental

2.1.   *Catalysts preparation*

Catalysts were prepared following an adapted method previously described in the literature [24]. A solution of cerium nitrate (1.7 mol.L^{-1}, 25 mL) was prepared, followed by the addition of an appropriate amount of nickel nitrate to obtain 10 wt% Ni in the catalyst. In another beaker, a solution of citric acid (6.7 mol.L^{-1}, 25 mL) was prepared, using a citric acid/metals molar ratio equal to 1.0. Both solutions were mixed and stirred for 2 h at room temperature. Then, the solution was heated at 70 °C under vacuum to remove water. The remaining material was dried at 100 °C overnight. The calcination occurred in 2 steps: 2 h at 300 °C and 4 h at 400 °C, using a heating rate of 1 °C/min. This catalyst was denominated Ni@CeO$_2$. The zirconia-doped ceria catalyst (Ni@CeZrO$_2$) was prepared using the same method with the addition of zirconyl nitrate at the metal solution. The Ce/Zr molar ratio was 4.0.

For comparison, a Ni/CeO$_2$ catalyst was prepared by incipient wetness impregnation of CeO$_2$ support with an aqueous solution of nickel nitrate. In this case, CeO$_2$ was synthesized by the method previously described but without the addition of nickel.

2.2.   *X-ray fluorescence (XRF)*

The chemical composition of the catalysts was determined by an X-ray fluorescence spectrometer RIGAKU RIX-3100 using samples as pellet.

2.3.   *N$_2$ physisorption*

The BET surface area of the samples was measured by N$_2$ adsorption using a Micromeritics Tristar 3000 apparatus at − 196 °C. The samples were degassed at 300 °C under vacuum before the analysis.

2.4.   Transmission electron microscopy (TEM)

TEM analyses of reduced and used catalysts were made in a JEOL 2100 UHR apparatus, with 0.19 and 0.14 nm punctual and linear resolution, respectively, equipped with a LaB_6 filament. Energy dispersive X-ray (EDX) analysis was also performed to determine the local chemical composition. The range used to collect the X-rays emitted from the sample upon electron impact was $0 - 20$ keV. Before the analysis, the samples were reduced at 800 °C for 1h, the same temperature used for the reaction.

2.5.   In-situ X-ray diffraction (XRD)

In-situ X-ray diffraction was performed at the XPD-10 B beamline at the Brazilian Synchroton Light Laboratory (LNLS). The samples were reduced under a 5 % H_2/He mixture at a heating rate of 10 °C/min, from 25 to 800 °C, remaining at the final reduction temperature for 1 h. The XRD patterns were obtained at 2θ range from 23° to 56° and the wavelength used was 1.55002 Å. The average crystallite size of NiO, metallic Ni and CeO_2 was calculated using the Scherrer equation. The CeO_2 lattice parameter was calculated using the Bragg's Law, assuming an orthorhombic structure and the *(111)* CeO_2 plane.

2.6.   In-situ X-ray absorption near edge structure (XANES)

XANES analysis was performed at the DXAS beamline at LNLS to obtain information about the reduction degree of Ni during the reduction procedure. The samples were diluted with boron nitride, used as inert, and pressed to obtain a pellet. The pellet was placed in a tubular reactor and reduced under a 5 % H_2/He mixture up to 750 °C, keeping this temperature for 30 min. The treatment of XANES data was carried out using PrestoPronto software [25]. The

fraction of metallic Ni phase was calculated as a function of reduction temperature by linear combination using NiO and Ni^0 foil XANES spectra as references.

2.7. $^{18}O_2/^{16}O_2$ isotopic exchange

The experiments were carried out in a closed recycling system connected to a Pfeiffer Vacuum quadrupole mass spectrometer and a vacuum pump. Firstly, the sample (c.a. 20 mg) was pre-treated under $^{16}O_2$ flow (50 mL/min, 500 °C, 1 h) and evacuated for 1 h. After the pre-treatment, the sample was cooled down to reaction temperature.

For the Isothermal Oxygen Isotopic Exchange (IOIE), the reactions occurred at 350 °C, 400 °C and 450 °C. It was inserted in the reactor 55 mbar of pure $^{18}O_2$ ($\geq$ 99 at.%, ISOTEC) and each isotopomer concentration was analyzed by monitoring the following m/z signals: 32 ($^{16}O_2$), 34 ($^{18}O^{16}O$), 36 ($^{18}O_2$).

The behavior of the oxygen exchange was studied as a function of the temperature (Temperature-Programmed Oxygen Isotopic Exchange – TPOIE). For this experiment, pure $^{18}O_2$ (55 mbar) was injected in the reactor at 200 °C and the sample was heated up to 500 °C (2 °C/min).

The following equations were used to calculate the rate of exchange (R_E), the number of oxygen exchanged (N_E), where Ng is the total number of oxygen atoms in the gas phase, w is the weight of catalyst, α_g^t is the atomic fraction of $^{18}O_2$ in the gas phase at the time t, α_g^0 is the initial atomic fraction of $^{18}O_2$ in the gas phase.

$$\propto_g^t = \frac{^1/_2\, P_{34}^t + P_{36}^t}{P_{36}^t + P_{34}^t + P_{32}^t} \qquad\qquad R_E = -N_g\, \frac{d \propto_g^t}{dt}\, x\, \frac{1}{w}$$

$$N_E = \left(\propto_g^0 - \propto_g^t\right) x\, N_g\, x\, \frac{1}{w}$$

2.8. Raman spectroscopy

The calcined samples were analyzed in a Raman Horiba Jobin Yvon spectrometer using a He:Ne laser (632 nm). The post-reaction samples were analyzed in a Raman Witec – Alpha 300 spectrometer. The 532 nm wavelength was used to observe the carbon structure on the samples.

2.9. Thermogravimetric analysis (TG)

In order to quantify the amount of coke formed on the catalyst, thermogravimetric analyses of the post-reaction samples were carried out in a TA Instruments equipment (SDT Q600). Approximately 10 mg of the spent catalyst was heated under synthetic air flow (100 mL/min) from room temperature to 1000 °C at a heating rate of 20 °C/min and the weight change was measured.

2.10. Scanning electron microscopy (SEM)

SEM analyses of the spent catalysts were carried out using a field emission scanning electron microscope (FE-SEM) Quanta FEG 450 FEI operating with an accelerating voltage of 20 kV.

2.11. Catalytic evaluation

Dry reforming of methane was performed in a fixed-bed reactor at atmospheric pressure. Before the reaction, the catalysts were reduced under pure H_2 (30 mL/min) at 800 °C for 1 h and purged under N_2 at the same temperature for 30 min. A reactant mixture with $CH_4:CO_2$ molar ratio equal to 1.0 under flow rate of 100 mL/min was used for the DRM at 800 ºC.

The samples (20 mg) were diluted with SiC (SiC mass/catalyst mass ratio = 1.5) to avoid hot spot or temperature gradients. The reaction products were analyzed by gas chromatography

(Agilent 6890) equipped with a thermal conductivity detector and Carboxen 1010 column (Supelco). The CH_4 and CO_2 conversion was determined as follow:

$$X_{CH_4} = \frac{(n_{CH_4})_{feed} - (n_{CH_4})_{exit}}{(n_{CH_4})_{feed}} \times 100$$

$$X_{CO_2} = \frac{(n_{CO_2})_{feed} - (n_{CO_2})_{exit}}{(n_{CO_2})_{feed}} \times 100$$

3. Results and discussion

3.1. Catalyst characterization

Table 1 shows the Ni content, Ce/Zr molar ratio and the textural properties of the catalysts. The Ni loading is close to the nominal value (10 wt%) for all samples, as well as the Ce/Zr molar ratio of the Ni@CeZrO$_2$ catalyst (i.e., Ce/Zr = 4). The surface area and pore volume for Ni/CeO$_2$ and Ni@CeO$_2$ catalysts were similar but decreased when zirconia was added to ceria. After the reduction process at 800 °C under H$_2$, the BET surface area dropped to less than 10 m^2/g to Ni/CeO$_2$ and Ni@CeO$_2$ catalysts. This reduction in the BET surface area can be correlated to sintering of CeO$_2$ at high temperature [26,27]. The decrease in BET surface area of Ni@CeZrO$_2$ sample was lower than that for the other samples. According to the literature [28], the addition of Zr into the ceria structure with the formation of a solid solution improves the thermal stability of the ceria support, inhibiting or minimizing sintering and surface area lost at high temperatures.

The TEM images of the reduced Ni/CeO$_2$, Ni@CeO$_2$ and Ni@CeZrO$_2$ catalysts are shown in Fig. 1. The image of Ni/CeO$_2$ catalyst shows large Ni particle segregated on the surface of the sample, with average particle size around 30 nm. The local chemical analysis showed only the presence of Ni due the large size and CeO$_2$ could not be detected in the area of analysis (white circle). For Ni@CeO$_2$ and Ni@CeZrO$_2$ catalysts, the TEM images reveals the presence of small Ni nanoparticles embedded in the ceria matrix formed during reduction. Segregated Ni particles could not be observed on the TEM images of Ni@CeO$_2$ and Ni@CeZrO$_2$ catalysts. Ni-embedded catalysts presented smaller metal particle size than Ni/CeO$_2$. For Ni@CeO$_2$ and Ni@CeZrO$_2$, the Ni particles sizes were around 13 and 6 nm, respectively. It was possible to detect the CeO$_2$ signal by EDX in the selected area (white circle) due the small Ni particle size and it seems that the nanoparticles embedded in the ceria matrix are protected.

The Raman spectra of the calcined samples are shown in Fig. 2. The spectrum of CeO_2 support is also presented for comparison. The support exhibits only one intense band at 462 cm^{-1} assigned to the symmetrical stretching mode between the eight oxygen atoms bound to the cerium atom in the triple degenerate F_{2g} mode. The impregnation of ceria with Ni does not affect the spectrum of Ni/CeO_2, but Ni@CeO_2 and Ni@$CeZrO_2$ samples show a ceria structure completely different from the impregnated one. Besides the intense band around 462 cm^{-1}, the spectra display bands at 224, 544 and 632 cm^{-1}, corresponding to second-order transverse acoustic mode (2TA) and defect-induced mode. These samples exhibited two different defects in the structure, which were reported in the literature as defect space including O^{2-} vacancy (544 cm^{-1}) and defect space without O^{2-} vacancy (632 cm^{-1}) [29,30]. The NiO also presents bands in the region of 570 cm^{-1} corresponding to TO and LO vibration modes [31]. However, this band is not detected or it has a very weak intensity in the spectrum of Ni/CeO_2 sample. Therefore, the bands observed at 544 cm^{-1} and 632 cm^{-1} in the spectra of Ni@CeO_2 and Ni@$CeZrO_2$ samples might be attributed to oxygen vacancies. Therefore, the one-step synthesis of the catalyst with Ni embedded in ceria structure can promote the formation of defect in the ceria, creating oxygen vacancies in its structure.

The Raman spectra did not detect the formation of a Ni-CeO_2 solid solution, as described by Barrio et al [32]. The formation of Ni-CeO_2 solid solution significantly shifted the frequency for the first-order F_{2g} peak to lower values, around 445 cm^{-1}. Then, the absence of the shift of this band for the Ni@CeO_2 catalyst shows that the Ni is embedded in CeO_2 structure instead of in a solid solution.

XANES experiments at the Ni K-edge were performed to study the reduction of nickel oxide for all samples (Figs. 3, 4 and 5). The XANES spectrum of the calcined Ni/CeO_2 sample shows the white line at 8352 eV characteristic of NiO. Increasing the reduction temperature under 5 % H_2/He mixture led to a continuous decrease in the intensity of this peak. At 450 °C,

12

the spectrum is characteristic of metallic Ni, indicating that nickel oxide was completely reduced to Ni^0. The same trend was observed for $Ni@CeO_2$ and $Ni@CeZrO_2$ catalysts as shown in Figs. 4 and 5.

However, the temperature range for the reduction of Ni oxide was different for the catalysts prepared by impregnation and sol-gel methods. Fig. 6 shows the evolution of the metallic Ni species during reduction calculated by the linear combination of Ni K-edge XANES spectra of references. The reduction of Ni/CeO_2 and $Ni@CeO_2$ samples starts at 290 and 277 °C, respectively, but at 190 °C for $Ni@CeZrO_2$ catalyst. The total reduction of nickel oxide on Ni/CeO_2 sample is achieved at 450 °C, while the complete reduction of the $Ni@CeO_2$ and $Ni@CeZrO_2$ samples occurs at higher temperatures (700 and 530 °C, respectively). The shift of reduction temperature to higher values is likely due to a higher metal-support interaction [32]. Therefore, these results suggest that nickel oxide particles embedded in the CeO_2 or $CeZrO_2$ matrix have stronger interaction with the support than nickel oxide particles impregnated on CeO_2. Stronger interaction demands higher temperature of reduction to remove oxygen from the oxide structure.

Fig. 7 shows the diffractograms of the calcined samples. Ni/CeO_2 and $Ni@CeO_2$ samples exhibit the characteristic lines of CeO_2 with fluorite structure (PDF 34-0394) at $2\theta = 28.7°$, 33.2° and 47.7°. The typical lines of NiO phase (PDF 47-1049) ($2\theta = 37.3°$ and 43.3°) are only detected for Ni/CeO_2 sample. The absence of diffraction lines ascribed to NiO phase in the diffractogram of $Ni@CeO_2$ sample can be attributed to the presence of very small NiO crystallites in this catalyst, indicating that sintering did not occur during the calcination. For $Ni@CeZrO_2$ sample, the lines characteristic of NiO phase are not detected either whereas the lines corresponding to CeO_2 are shifted to higher 2θ positions. The partial substitution of Ce^{4+} by Zr^{4+} ions in the ceria structure shifted the CeO_2 lines to higher Bragg angles that corresponds to a decrease in the lattice parameter (Table 2) due to the difference between the

13

ionic radii of the cations Ce^{4+} (0.97 Å) and Zr^{4+} (0.84 Å) [33]. According to the literature, this shift indicates the formation of a CeO_2-ZrO_2 solid solution for the Ni@CeZrO$_2$ catalyst [18,34]. Ni/CeO$_2$ catalyst exhibited a ceria lattice parameter higher than that one reported in the literature (5.4112 Å), while it further decreased for Ni@CeO$_2$ with Ni embedded in CeO_2. The CeO_2 crystallite size of the Ni/CeO$_2$ sample is 13.4 nm, while a significant decrease is observed for Ni@CeO$_2$ and Ni@CeZrO$_2$ catalysts (4.4 and 4.1 nm, respectively) (Table 2). Wang et al. [24] synthesized a Cu@CeO$_2$ catalyst using the same method and they observed the same effect on ceria crystallite size during calcination.

X-ray diffraction patterns obtained during reduction under 5 % H$_2$/He mixture from room temperature to 800 °C for Ni/CeO$_2$, Ni@CeO$_2$ and Ni@CeZrO$_2$ samples are shown in Figs. 8A, 9A and 10A. The evolution of the mean crystallite size of NiO, Ni^0 and CeO$_2$ during reduction procedure is presented in Figs. 8b, 9b and 10b.

For Ni/CeO$_2$ catalyst (Fig. 8A), the diffractograms show the decrease in the intensities of the lines corresponding to NiO at $2\theta = 37.3°$ and $43.3°$ during reduction. Above 300 °C, the typical lines of NiO disappear and a new line is observed at $2\theta = 44.5°$, corresponding to metallic Ni phase (PDF 4-850). Further heating up to 800 °C and isothermal period of 1h at this temperature led to an increase in the intensities of the characteristic lines of Ni^0 and CeO$_2$. These results suggest a sintering of CeO$_2$ and Ni^0 crystallites during the reduction, as shown in Fig. 8B. The crystallite size of CeO$_2$ increased from 12 nm (580 °C) to 65 nm (800 °C for 1h), whereas the Ni^0 crystallite size grew from 5 nm (300 °C) to 33 nm (800 °C for 1h).

For Ni@CeO$_2$ and Ni@CeZrO$_2$ catalysts, only the typical lines of CeO$_2$ are observed below 500 °C. Above this temperature, the appearance of the lines corresponding to metallic Ni is noticed at 525 °C and 600 °C on the diffractograms of Ni@CeO$_2$ and Ni@CeZrO$_2$ catalysts, respectively. These results reveal that the reduction of nickel oxide is more difficult for the samples prepared by the sol-gel method, which is likely due to the strong interaction between

14

nickel oxide and CeO_2. These results agree with the TEM images and *in situ* XANES experiments, which showed that the embedded Ni particles in the ceria matrix are more hardly reduced than the segregated particles characteristic of the impregnated catalyst. The strong interaction between Ni and CeO_2 has been reported as an approach to improve the dispersion and avoid the metal sintering at high temperature [35]. Kathiraser at al. [36] studied the influence of Ce addition to Ni/SiO_2 catalysts for the oxidative reforming of biogas. They observed the increase in NiO reduction temperature with the presence of small amount of Ce (0.5 wt%) in the catalyst. This result was attributed to a higher interaction $Ni-CeO_2$ than $Ni-SiO_2$ as well as to a smaller NiO crystallite size as revealed by EXAFS. The TPR peaks of $Ni@SiO_2$ core-shell structure were shifted to higher temperatures in comparison to Ni/SiO_2 indicating that nickel oxide was hardly reduced in the core-shell structure [37]. This result was associated with a stronger metal-support interaction.

For $Ni@CeO_2$, the CeO_2 crystallite size increased during the reduction from 5 nm (325 °C) to 68 nm (800 °C for 1h), revealing a strong sintering at high temperature even for this sample prepared by the sol-gel method (Fig. 9B). A significant growth of the Ni^0 crystallite size was also observed, increasing from 5 nm (630 °C) to 19 nm (800 °C for 1h).

In the case of $Ni@CeZrO_2$ catalyst, the CeO_2 crystallite size only slightly varied from 5 to 8 nm after reduction at 800 °C for 1h. The same trend was observed for the Ni^0 crystallite size that increased from 5 to 10 nm at the end of the reduction (Fig. 10B).

The values of BET surface area of the samples before and after reduction (Table 1) showed that the addition of Zr into ceria structure significantly improved the thermal stability of the $Ni@CeZrO_2$ catalyst. The effect of type of dopant on the thermal stability and redox properties of ceria has been studied in the literature [20,38,39]. A higher thermal stability of $CeZrO_2$ in comparison to CeO_2 was attributed to the formation of a CeZr solid solution [28]. The samples aged at 1000 °C under reduction condition showed CeO_2 crystallite size equal to

73 and 39, for Pt/CeO$_2$ and Pt/Ce$_{0.75}$Zr$_{0.25}$O$_2$, respectively. In our work, the higher thermal stability of the ceria structure is likely due to the formation of the CeZrO$_2$ solid solution as revealed by XRD.

The increase in the reduction temperature led to a shift of the ceria lines to lower angles. The variation of CeO$_2$ lattice parameter during reduction of the samples is shown in Fig. 11. Increasing the reduction temperature increased the lattice parameter. The increase in the lattice parameter could be due to the thermal expansion as well as the change in the oxidation state of ceria from Ce^{4+} to Ce^{3+}. In order to evaluate the effect of thermal expansion on the ceria lattice parameter during the reduction of all catalysts, an experiment was carried out with a physical mixture containing NiO and CeO$_2$ (Sigma-Aldrich) under air. The linear increase in the lattice parameter of NiO-CeO$_2$ up to 700 °C (see dotted line in Fig. 11) is attributed to the thermal expansion of the samples. However, the curves obtained for Ni/CeO$_2$, Ni@CeO$_2$ and Ni@CeZrO$_2$ catalysts deviates from this linear increase of the lattice parameter above 200 °C, indicating that the reduction of ceria began. Furthermore, a sharp increase in the lattice parameter was observed for Ni/CeO$_2$ and Ni@CeO$_2$ catalysts around 700 °C. The ceria reduction at low temperature region is generally attributed to the reduction of surface ceria, whereas the reduction at high temperature corresponds to the ceria bulk reduction [40]. The non-linear increase of the lattice parameter with the reduction temperature is likely due to the conversion of Ce^{4+} to Ce^{3+} [32]. Ce^{3+} ions have a higher ionic radius (1.034 Å) as compared to the Ce^{4+} ions (0.92 Å). Then, the formation of Ce^{3+} ions in ceria structure causes a change in the Ce-O bond length, which produces a lattice expansion and create oxygen vacancies [41]. The higher variation of lattice parameter for Ni@CeO$_2$ and Ni@CeZrO$_2$ suggests the formation of a higher number of oxygen vacancies on these catalysts during reduction.

The TPOIE experiments (Fig. 12) were performed to investigate the oxygen exchange capacity of the support as a function of temperature. The CeO$_2$ support only starts to exchange

oxygen at 380 °C, reaching the value of 39 x 10^{20} at.g^{-1}. The oxygen exchange begins at around 280 °C for Ni/CeO$_2$ catalyst and it occurs until Ne = 35 x 10^{20} at.g^{-1} at 500 °C. For the embedded Ni@CeO$_2$ catalyst, the exchange started at lower temperature compared to the impregnated one (250 °C). At 500 °C, the number of exchanged oxygen atoms is 39 x 10^{20} at.g^{-1}. In comparison to Ni/CeO$_2$ and Ni@CeO$_2$ catalysts, the oxygen exchange begin at higher temperature for Ni@CeZrO$_2$ (300 °C) and the number of O atoms exchanged at 500 °C was 42 x 10^{20} at.g^{-1}. Da Silva et al. [39] have reported similar results for CeO$_2$ and CeNb supports. The catalysts showed similar isotopic distribution during the experiment (Fig. 13), indicating the occurrence of simple and multiple heteroexchange mechanisms [42].

The presence of metal decreases the energy required to start the exchange process compared with the CeO$_2$ support, because the exchange will occur mainly through the metal particle [43]. The doping of CeO$_2$ by ZrO$_2$ increases the temperature in which the exchange start. This delay can be associated with a decrease in the surface oxygen concentration due to the lower specific surface area of CeZrO$_2$ compared to CeO$_2$. On the contrary there is a fast increase in the number of atoms exchanged for Ni@CeZrO$_2$, indicating that more oxygen atoms from the bulk phase are participating in the exchange process when Zr^{4+} is inserted into the CeO$_2$ structure. Therefore, the Ni@CeZrO$_2$ catalyst exhibited the highest number of oxygen exchanged compared with Ni/CeO$_2$ and Ni@CeO$_2$.

The experiments of isotopic oxygen exchange were carried out at 350, 400 and 450 °C. Figs. 14 and 15 illustrate the evolution of the number of exchanged atoms (N$_e$) and the isotopic distribution which occurs during the experiment at 400 °C. Table 3 reports the initial rate of exchange calculated from IOIE for the three temperatures. The exchange for CeO$_2$ is very low compared with the samples containing Ni, because the metal promotes the spillover of oxygen to ceria surface, as observed also in the TPOIE experiment. Comparing the Ni/CeO$_2$ and Ni@CeO$_2$ catalysts, the presence of Ni nanoparticles embedded on ceria structure does not

17

affect significantly the number of O atoms exchanged at the gas/solid equilibrium, but it increases significantly the initial rate of exchange, showing the positive influence of the close contact between Ni nanoparticles and ceria support (Table 3). The lower initial exchange rate and the higher N_e after 20 min reaction that are observed for Ni@CeZrO$_2$ catalyst confirms the results obtained in TPOIE experiment: a lower surface exchange activity compared to ceria-based samples but a higher bulk diffusion.

Indeed, the Ni@CeZrO$_2$ catalyst showed the highest number of N_e and the percentage of O atoms exchanged (Table 4). Furthermore, this catalyst exhibits a different behavior in the beginning of exchange at each temperature, with more formation of $^{32}O_2$ than $^{34}O_2$. On the opposite, Ni/CeO$_2$ and Ni@CeO$_2$ catalysts had a simultaneous formation of $^{32}O_2$ and $^{34}O_2$. Then, the Ni@CeZrO$_2$ catalyst favors the multiple exchange in comparison to the simple exchange at the beginning. Multiple heteroexchange occurs when two oxygen atoms are exchanged at the same time. Duprez et al. [42] observed the same behavior for Ce$_{0.76}$Zr$_{0.32}$O$_2$ samples, which was attributed to a higher concentration of superoxides species (O$_2^-$) at the surface of the samples after oxidizing pre-treatment. Rossignol et al. [44] also correlated the presence of these species to the higher oxygen storage capacity when the Zr^{4+} is inserted in the ceria structure.

3.2. DRM reaction

The evolution of the CH$_4$ conversion, CO$_2$ conversion and H$_2$/CO molar ratio as a function of time on stream (TOS) at 800 ºC are presented in Figs. 16A, 16B and 16C. The initial CH$_4$ and CO$_2$ conversions were approximately the same for all catalysts and they remained quite constant during 24 h of TOS. The reaction produces H$_2$ and CO with a H$_2$/CO molar ratio around 0.8. The CO$_2$ conversion was higher than the CH$_4$ conversion due to the occurrence of

18

reverse water gas shift reaction (Eq. 1.4), leading to the production of CO and H_2O and consequently, the H_2/CO ratio was lower than 1.0.

3.3. Characterization of used catalysts after DRM reaction

The main challenge on the design of a catalyst for the DRM reaction concerns the deactivation caused by carbon deposition. In order to investigate the formation of carbon during DRM reaction, the spent catalysts were characterized by SEM, TEM, Raman and TGA analysis.

SEM images of the catalysts after DRM at 800 °C for 24 h of TOS are displayed in Fig. 17. SEM image revealed the presence of carbon filaments on Ni/CeO_2 and $Ni@CeO_2$, mainly on the catalyst prepared by impregnation. On the other hand, carbon filaments were hardly detected on $Ni@CeZrO_2$ catalyst.

The TEM images of used catalysts shown in Fig. 18 can provide information about metal sintering as well as the formation of carbon filaments during the reaction. Ni/CeO_2 catalyst (Figs. 18 A and B) presented Ni nanoparticles without any interaction with CeO_2 matrix. Some Ni nanoparticles are located inside the carbon filaments, which avoid their sintering. There are also large nanoparticles outside the carbon nanotubes with particle size around 40 nm. For $Ni@CeO_2$ catalyst (Figs. 18 C and D), TEM images reveal the presence of Ni nanoparticles into CeO_2 bulk but sintering is observed (Ni particle size around 20 nm). This higher interaction inhibits the detachment of Ni particles from CeO_2 and the growth of carbon filament. The TEM images of $Ni@CeZrO_2$ (Figs. 18 E and F) show Ni nanoparticles embedded into ceria matrix with very small particle size (around 8 nm) after 24 h of TOS. Furthermore, carbon filaments are not observed, which demonstrate that inhibiting Ni sintering in the presence of a support with oxygen mobility suppress the formation of carbon filaments.

The Raman spectra of used catalysts exhibit two bands in the range of 1200 to 1800 cm^{-1}, which are indicative of carbon formation (Fig. 19). The G-band at 1581 cm^{-1} is indicative of

ordered carbon, whereas the band at 1350 cm^{-1} (D-band) has been related to disordered carbon structures [45]. The D-band in the range of 1285-1300 cm^{-1} is ascribed to single-walled carbon nanotubes (SWCNT), while the position around 1330 cm^{-1} is related to multi-walled carbon nanotubes (MWCNT) or crystalline graphite-like forms [46,47]. The position of the D-band in 1350 cm^{-1} and the SEM images suggest the presence of MWCNT. Furthermore, the intensity of these bands was higher for Ni/CeO$_2$, indicating that the highest carbon deposition took place on this catalyst. These bands are barely detected on the spectrum of Ni@CeZrO$_2$, which suggests the presence of very low amount of carbon deposits on this catalyst, in agreement with the SEM image.

The derivative of weight during the TGA analysis is shown in Fig. 20. The DTG profile of Ni/CeO$_2$ sample exhibited an intense peak at 614 °C, whereas a broad peak at 518 °C is observed in the DTG profile of Ni@CeO$_2$ catalyst. No peak was detected on the DTG profile of Ni@CeZrO$_2$, indicating that carbon was not deposited on this catalyst.

Table 5 reports the average rate of carbon formation for each catalyst during DRM reaction at 800 °C for 24 h of TOS. Ni/CeO$_2$ catalyst exhibited the highest amount of carbon deposits but the carbon formation rate was significantly reduced for the catalysts containing Ni nanoparticles embedded in ceria structure. Ni@CeZrO$_2$ catalyst did not show evidences of carbon formation after DRM reaction.

3.4. The effect of Ni embedded in CeO$_2$ on catalyst deactivation for DRM

The mechanism of carbon formation over Ni-based catalysts during DRM has been extensively discussed in the literature [7,48,49] and involves the dissociation of methane on the surface of nickel particles, producing hydrogen and carbon (C$_\alpha$). In the presence of a support with redox properties such as ceria and ceria-zirconia mixed oxides, this highly reactive carbon species (C$_\alpha$) may reacts with oxygen from the support producing CO [46,50,51]. The unbalance

20

between the rate of methane decomposition and the reaction rate of carbon with oxygen from the support will lead to the accumulation of a less active carbon (C_β) that may also migrate into the nickel particle producing carbon filaments. Furthermore, the oxygen vacancies in the catalysts acts like active sites for CO_2 dissociative adsorption, which increase the amount of oxygen species on its surface. Therefore, the support plays an important role on the DRM reaction, keeping the metal surface free of carbon deposits. Yan et al. [52] recently demonstrated the importance of reactive oxygen species in close contact with Ni nanoparticles to oxidize the C_α before its polymerization for Ni/CeO_2-SiO_2 catalysts. The conversion of C_α species to CO by the reactive oxygen species could enhance the catalytic properties and stability of the Ni/CeO_2-SiO_2 catalyst. The same result was reported by Marinho et al. [50] for the steam reforming of ethanol over $LaNiO_3$/$CeSiO_2$ precursor catalyst. The strong metal-support interaction favored the transfer of oxygen from the support to metal through the metal-support interface. Roh et al. [53] successfully synthetized Ni catalyst supported on CeO_2-ZrO_2 solid solution. They could observe the enhancement on catalyst stability for Ni/$Ce_{0.8}Zr_{0.2}O_2$, which was due to the higher oxygen storage capacity and Ni dispersion. Yentekakis et al. [17] also proposed that $CeZrO_2$ support promotes the dissociative adsorption of CO_2, producing a labile lattice oxygen that contributes to carbon oxidation.

Moreover, the rate of carbon formation is strongly affected by the Ni crystallite size [10]. The initiation step of carbon formation is more difficult over smaller particles. Then, carbon formation is minimized or inhibited on catalysts with small Ni particle sizes. Wang et al. [37] showed that the confinement of Ni nanoparticles inside SiO2 spheres on Ni@SiO_2 inhibited metal sintering during dry reforming of methane, minimizing carbon formation. Pu et al. [14] evaluated the influence of Ce on Ni@Al_2O_3 core-shell catalysts to improve the coke resistance for steam reforming of acetic acid. The Ni@Al_2O_3 core-shell structure could avoid metal sintering (Ni crystallite size < 5 nm) but carbon formation was observed yet. However,

the addition of Ce suppressed carbon deposition, which was attributed to the oxygen mobility of the material. The combination of small Ni size with oxygen mobility was fundamental to design a catalyst resistant to carbon formation.

In our work, the slight decrease in CH_4 and CO_2 conversions is likely due to the growth of Ni particle size as revealed by TEM. Furthermore, the inclusion of Ni nanoparticles into the $CeZrO_2$ structure for Ni@$CeZrO_2$ catalyst reduced metal sintering, as revealed by *in situ* XRD and TEM, due to the thermal stability of $CeZrO_2$ support during the reduction pre-treatment. In addition, this catalyst exhibited the highest number of O atoms exchanged during the isothermal oxygen isotopic exchange at 400 °C as well as the highest amount of oxygen vacancies formed as shown by XRD and Raman spectroscopy. Therefore, the control of Ni particle size and the high oxygen mobility of Ni@$CeZrO_2$ catalyst inhibited carbon deposition and favored the mechanism of carbon removal, promoting catalyst stability.

4.Conclusions

The one step preparation of Ni@CeO_2 and Ni@$CeZrO_2$ catalysts led to Ni nanoparticles embedded in the oxide, which had a positive effect on the stabilization of the Ni particle size during the reduction at high temperature (800 °C). It also generates more oxygen vacancies and increases the interaction with $CeZrO_2$ and CeO_2 in comparison with an impregnated catalyst Ni/CeO_2. Furthermore, doping of ceria with Zr could maintain the ceria structure throughout the thermal treatment and increase the mobility of oxygen in the material, compared to ceria alone, favoring the carbon removal mechanism during the reaction. Thus, the protection of the metal particle against sintering as well as the oxidation of carbon species by the support for the catalyst Ni@$CeZrO_2$ resulted in the suppression of carbon deposition during the DRM in our work.

5. Acknowledgements

6. References

[1]   I.V. Yentekakis, G. Goula, Biogas Management: Advanced Utilization for Production of Renewable Energy and Added-value Chemicals, Front. Environ. Sci. 5 (2017) 7.

[2]   Y. Gao, J. Jiang, Y. Meng, F. Yan, A. Aihemaiti, A review of recent developments in hydrogen production via biogas dry reforming, Energy Conversion and Management 171 (2018) 133–155.

[3]   T.M. Gür, Comprehensive review of methane conversion in solid oxide fuel cells: Prospects for efficient electricity generation from natural gas, Progress in Energy and Combustion Science 54 (2016) 1–64.

[4]   H.N.C. da Silva, D.M. Prata, G.B.A. Lima, L.P. Zotes, L.V. Mattos, A techno-economic evaluation of the energy generation by proton exchange membrane fuel cell using biogas reforming, Journal of Cleaner Production, 200 (2018) 598-608.

[5]   L. Yang, X. Ge, C. Wan, F. Yu, Y. Li, Progress and perspectives in converting biogas to transportation fuels, Renew. Sustain. Energy Rev. 40 (2014) 1133–1152.

[6]   S.M. Stagg-Williams, F.B. Noronha, G. Fendley, D.E. Resasco, CO_2 reforming of CH_4 over Pt/ZrO_2 catalysts promoted with La and Ce oxides, J. Catal. 194 (2000) 240-249.

23

[7]   M.C.J. Bradford, M.A. Vannice, CO_2 reforming of CH_4, Catal. Rev. - Sci. Eng. 41 (1999) 1-42.

[8]   J. Rostrup-Nielsen, J.-H. Bak Hansen, CO_2 Reforming of Methane over Transition Metals, J. Catal. 144 (1993) 38–49.

[9]   P.M. Mortensen, I. Dybkjaer, Industrial scale experience on steam reforming of CO_2-rich gas, Appl. Catal. A: General 495 (2015) 141–151.

[10] R.C. Rabelo-Neto, H.B.E. Sales, C.V.M. Inocêncio, E. Varga, A. Oszko, A. Erdohelyi, F.B. Noronha, L.V. Mattos, CO_2 reforming of methane over supported LaNiO3 perovskite-type oxides, Appl. Catal. B: Environ. 221 (2018) 349–361.

[11] M. Cargnello, N.L. Wieder, T. Montini, R.J. Gorte, P. Fornasiero, Synthesis of dispersible $Pd@CeO_2$ core-shell nanostructures by self-assembly, J. Am. Chem. Soc. 132 (2010) 1402–1409.

[12] A.J. Majewski, J. Wood, Tri-reforming of methane over $Ni@SiO_2$ catalyst, Int. J. Hydrog. Energy. 39 (2014) 12578–12585.

[13] C.S. Bonifacio, S. Carenco, C.H. Wu, S.D. House, H. Bluhm, J.C. Yang, Thermal Stability of Core–Shell Nanoparticles: A Combined in Situ Study by XPS and TEM, Chem. Mater. 27 (2015) 6960–6968.

[14] J. Pu, Y. Luo, N. Wang, H. Bao, X. Wang, E.W. Qian, Ceria-promoted $Ni@Al_2O_3$ core-shell catalyst for steam reforming of acetic acid with enhanced activity and coke resistance, Int. J. Hydrog. Energy. 43 (2018) 3142–3153.

[15] F. Wang, B. Han, L. Zhang, L. Xu, H. Yu, W. Shi, CO_2 reforming with methane over small-sized $Ni@SiO_2$ catalysts with unique features of sintering-free and low carbon, Appl. Catal. B Environ. 235 (2018) 26–35.

[16] Q. Huang, X. Fang, Q. Cheng, Q. Li, X. Xu, L. Xu, W. Liu, Z. Gao, W. Zhou, X. Wang, Synthesis of a Highly Active and Stable Nickel-Embedded Alumina Catalyst for Methane

Dry Reforming: On the Confinement Effects of Alumina Shells for Nickel Nanoparticles, ChemCatChem. 9 (2017) 3563–3571.

[17] X. Wang, J.A. Rodriguez, J.C. Hanson, D. Gamarra, A. Martínez-Arias, M. Fernández-García, Ceria-based catalysts for the production of H_2 through the water-gas-shift reaction: Time-resolved XRD and XAFS studies, Top. Catal. 49 (2008) 81–88.

[18] E.C. Faria, R.C.R. Neto, R.C. Colman, F.B. Noronha, Hydrogen production through CO_2 reforming of methane over $Ni/CeZrO_2/Al_2O_3$ catalysts, Catal. Today 228 (2014) 138–144.

[19] S. Bedrane, C. Descorme, D. Duprez, Investigation of the oxygen storage process on ceria- and ceria – zirconia-supported catalysts, Catal. Today 75 (2002) 401–405.

[20] P.P. Silva, F.A. Silva, L.S. Portela, L.V. Mattos, F.B. Noronha, C.E. Hori, Effect of Ce/Zr ratio on the performance of $Pt/CeZrO_2/Al_2O_3$ catalysts for methane partial oxidation, Catal. Today 107 (2005) 734–740.

[21] I.V. Yentekakis, G. Goula, M. Hatzisymeon, I. Betsi-Argyropoulou, G. Botzolaki, K. Kousi, D.I. Kondarides, M.J. Taylor, C.M.A. Parlett, A. Osatiashtiani, G. Kyriakou, J.P. Holgado, R.M. Lambert, Effect of support oxygen storage capacity on the catalytic performance of Rh nanoparticles for CO_2 reforming of methane, Appl. Catal. B Environ. 243 (2019) 490–501.

[22] A. Wolfbeisser, O. Sophiphun, J. Bernardi, J. Wittayakun, K. Föttinger, G. Rupprechter, Methane dry reforming over ceria-zirconia supported Ni catalysts, Catal. Today 277 (2016) 234–245.

[23] E.T. Saw, U. Oemar, M.L. Ang, K. Hidajat, S. Kawi, Highly Active and Stable Bimetallic Nickel-Copper Core-Ceria Shell Catalyst for High-Temperature Water-Gas Shift Reaction, ChemCatChem. 7 (2015) 3358–3367.

[24] Y. Wang, Y. Zhao, J. Lv, X. Ma, Facile synthesis of $Cu@CeO_2$ and its catalytic behavior for hydrogenation of methyl acetate to ethanol, ChemCatChem. 9 (2017) 2085–2090.

[25] S.J.A. Figueroa, C. Prestipino, PrestoPronto: a code devoted to handling large data sets, J. Phys. Conf. Ser. 712 (2016) 12–16.

[26] M. Li, A.C. van Veen, Tuning the catalytic performance of Ni-catalysed dry reforming of methane and carbon deposition via Ni-CeO$_{2-x}$ interaction, Appl. Catal. B Environ. 237 (2018) 641–648.

[27] H. Ay, D. Üner, Dry reforming of methane over CeO$_2$ supported Ni, Co and Ni–Co catalysts, Appl. Catal. B Environ. 179 (2015) 128–138.

[28] C.E. Hori, H. Permana, K.Y.S. Ng, A. Brenner, K. More, K.M. Rahmoeller, D. Belton, Thermal stability of oxygen storage properties in a mixed CeO$_2$-ZrO$_2$ system, Appl. Catal. B-Environ. 16 (1998) 105–117.

[29] T. Taniguchi, T. Watanabe, N. Sugiyama, A.K. Subramani, H. Wagata, N. Matsushita, M. Yoshimura, Identifying defects in ceria-based nanocrystals by UV resonance Raman spectroscopy, J. Phys. Chem. C. 113 (2009) 19789-19793.

[30] A. Nakajima, ~ A Yoshihara, M. Ishigame, Defect-induced Raman spectra in doped CeO$_2$, Phys. Rev. B. 50 (1994) 13297-13307.

[31] N. Mironova-Ulmane, A. Kuzmin, I. Steins, J. Grabis, I. Sildos, M. Pärs, Raman scattering in nanosized nickel oxide NiO, J. Phys. Conf. Ser. 93 (2007) 1-5.

[32] L. Barrio, A. Kubacka, G. Zhou, M. Estrella, A. Martínez-Arias, J.C. Hanson, M. Fernández-García, J.A. Rodriguez, Unusual Physical and Chemical Properties of Ni in Ce$_{1-x}$Ni$_x$O$_{2-y}$ Oxides: Structural Characterization and Catalytic Activity for the Water Gas Shift Reaction, J. Phys. Chem. C. 114 (2010) 12689–12697.

[33] A. Bonk, A. Remhof, A.C. Maier, M. Trottmann, M.V.F. Schlupp, C. Battaglia, U.F. Vogt, Low-Temperature Reducibility of M$_x$Ce$_{1-x}$O$_2$ (M = Zr, Hf) under Hydrogen Atmosphere, J. Phys. Chem. C. 120 (2015) 118–125.

[34] A.I. Kozlov, H.K. Do, A. Yezerets, P. Andersen, H.H. Kung, M.C. Kung, Effect of preparation method and redox treatment on the reducibility and structure of supported ceria-zirconia mixed oxide, J. Catal. 209 (2002) 417–426.

[35] W. Zheng, J. Zhang, Q. Ge, H. Xu, W. Li, Effects of CeO_2 addition on Ni/Al_2O_3 catalysts for the reaction of ammonia decomposition to hydrogen, Appl. Catal. B Environ. 80 (2008) 98–105.

[36] Y. Kathiraser, Z. Wang, M.L. Ang, L. Mo, Z. Li, U. Oemar, S. Kawi, Highly active and coke resistant Ni/SiO_2 catalysts for oxidative reforming of model biogas: Effect of low ceria loading, J. CO_2 Util. 19 (2017) 284–295.

[37] F. Wang, L. Xu, W. Shi, Syngas production from CO_2 reforming with methane over core-shell $Ni@SiO_2$ catalysts, J. CO_2 Util. 16 (2016) 318–327.

[38] J. Kašpar, P. Fornasiero, M. Graziani, Use of CeO_2-based oxides in the three-way catalysis, Catal. Today. 50 (1999) 285–298.

[39] A.A.A. da Silva, N. Bion, F. Epron, S. Baraka, F.C. Fonseca, R.C. Rabelo-Neto, L.V. Mattos, F.B. Noronha, Effect of the type of ceria dopant on the performance of Ni/CeO_2 SOFC anode for ethanol internal reforming, Appl. Catal. B Environ. 206 (2017) 626–641.

[40] V. Perrichon, A. Laachir, G. Bergeret, R. Fréty, L. Tournayan, O. Touret, Reduction of ceria with different textures by hydrogen and their reoxidation by oxygen, J. Chem. Soc. Faraday Trans. 90 (1994) 773–781.

[41] M. Piumetti, S. Bensaid, D. Fino, N. Russo, Nanostructured ceria-zirconia catalysts for CO oxidation: Study on surface properties and reactivity, Appl. Catal. B Environ. 197 (2016) 35–46.

[42] Y. Madier, C. Descorme, A.M. Le Govic, D. Duprez, Oxygen Mobility in CeO_2 and $Ce_xZr_{(1-x)}O_2$ Compounds: Study by CO Transient Oxidation and $^{18}O/^{16}O$ Isotopic Exchange, J. Phys. Chem. B. 103 (1999) 10999–11006.

[43] D. Martin, D. Duprez, Mobility of Surface Species on Oxides. 1. Isotopic Exchange of $^{18}O_2$ with ^{16}O of SiO_2, Al_2O_3, ZrO_2, MgO, CeO_2, and CeO_2-Al_2O_3. Activation by Noble Metals. Correlation with Oxide Basicity, J. Phys. Chem. 100 (1996) 9429–9438.

[44] S. Rossignol, F. Gérard, D. Duprez, Effect of the preparation method on the properties of zirconia-ceria materials, J. Mater. Chem. 9 (1999) 1615–1620.

[45] W.E. Alvarez, F. Pompeo, J.E. Herrera, L. Balzano, D.E. Resasco, Characterization of single-walled carbon nanotubes (SWNTs) produced by CO disproportionation on Co-Mo catalysts, Chem. Mater. 14 (2002) 1853-1858.

[46] O.C.V. Silva, E.B. Silveira, R.C. Rabelo- Neto, L.E.P. Borges, F.B. Noronha, Hydrogen Production Through Steam Reforming of Toluene Over Ni Supported on MgAl Mixed Oxides Derived from Hydrotalcite-Like Compounds, Catal. Letters. 148 (2018) 1622–1633.

[47] T. Belin, F. Epron, Characterization methods of carbon nanotubes: a review, Mater. Sci. Eng. B. 119 (2005) 105–118.

[48] P. Ferreira-Aparicio, Mechanistic aspects of the dry reforming of methane over ruthenium catalysts, Appl. Catal. A 202 (2000) 183–196.

[49] J. Wei, E. Iglesia, Isotopic and kinetic assessment of the mechanism of reactions of CH_4 with CO_2 or H_2O to form synthesis gas and carbon on nickel catalysts, J. Catal. 224 (2004) 370–383.

[50] A.L.A. Marinho, R.C. Rabelo-Neto, F.B. Noronha, L. V. Mattos, Steam reforming of ethanol over Ni-based catalysts obtained from $LaNiO_3$ and $LaNiO_3$/$CeSiO_2$ perovskite-type oxides for the production of hydrogen, Appl. Catal. A 520 (2016) 53–64.

[51] F.B. Noronha, E.C. Fendley, R.R. Soares, W.E. Alvarez, D.E. Resasco, Correlation between catalytic activity and support reducibility in the CO_2 reforming of methane over $Pt/Ce_xZr_{1-x}O_2$ catalysts, Chem. Eng. J. 82 (2001) 21–31.

[52] X. Yan, T. Hu, P. Liu, S. Li, B. Zhao, Q. Zhang, W. Jiao, S. Chen, P. Wang, J. Lu, L. Fan, X. Deng, Y. X. Pan, Highly efficient and stable Ni/CeO$_2$-SiO$_2$ catalyst for dry reforming of methane: Effect of interfacial structure of Ni/CeO$_2$ on SiO$_2$, Appl. Catal. B Environ. 246 (2019) 221–231.

[53] H.-S. Roh, K.Y. Koo, U.D. Joshi, W.L. Yoon, Combined H$_2$O and CO$_2$ Reforming of Methane Over Ni–Ce–ZrO$_2$ Catalysts for Gas to Liquids (GTL), Catal. Lett. 125 (2008) 283–288.

Figure Caption

Figure 1. TEM images and EDX of selected areas of Ni/CeO_2, $Ni@CeO_2$ and $Ni@CeZrO_2$ catalysts after reduction at 800 °C.

Figure 2. Raman spectra for the calcined samples and a CeO_2 reference.

Figure 3. XANES spectra obtained during the reduction of Ni/CeO_2 catalyst.

Figure 4. XANES spectra obtained during the reduction of $Ni@CeO_2$ catalyst.

Figure 5. XANES spectra obtained during the reduction of $Ni@CeZrO_2$ catalyst.

Figure 6. Fraction of Ni^0 calculated by the linear combination of Ni K-edge XANES spectra of references during the reduction for all catalysts.

Figure 7. X-ray diffraction patterns of calcined samples: (A) Ni/CeO_2; (B) $Ni@CeO_2$; and (C) $Ni@CeZrO_2$.

Figure 8. (A) X-ray diffraction patterns obtained during reduction from room temperature to 800 °C for Ni/CeO_2; (B) Crystallite size of NiO, Ni^0 and CeO_2 during the reduction process.

Figure 9. (A) X-ray diffraction patterns obtained during reduction from room temperature to 800 °C for $Ni@CeO_2$; (B) Crystallite size of Ni^0 and CeO_2 during the reduction process.

Figure 10. (A) X-ray diffraction patterns obtained during reduction from room temperature to 800 °C for $Ni@CeZrO_2$; (B) Crystallite size of Ni^0 and CeO_2 during the reduction process.

Figure 11. Variation of CeO_2 lattice parameter as a function of reduction temperature for all catalysts; (---) $NiO-CeO_2$ physical mixture; (●) Ni/CeO_2; (▲) $Ni@CeO_2$; (▼) $Ni@CeZrO_2$.

Figure 12. Evolution of the number of exchanged oxygen atoms during TPOIE over Ni/CeO_2, $Ni@CeO_2$, $Ni@CeZrO_2$ and CeO_2.

Figure 13. Isotopic distribution during the TPOIE for Ni/CeO_2, $Ni@CeO_2$, $Ni@CeZrO_2$ and CeO_2.

Figure 14. Evolution of the number of exchanged oxygen atoms during IOIE at 400 °C over CeO_2, Ni/CeO_2, $Ni@CeO_2$ and $Ni@CeZrO_2$.

Figure 15. Isotopic distribution during the IOIE at 400 °C.

Figure 16. (A) CH_4 conversion, (B) CO_2 conversion and (C) H_2/CO molar ratio versus TOS for dry reforming at 800 °C.

Figure 17. SEM images of spent catalysts after DRM at 800 °C for 24 h of TOS.

Figure 18. TEM images of spent catalysts after DRM at 800 °C for 24 h of TOS; (A) and (B) Ni/CeO_2; (C) and (D) $Ni@CeO_2$; (E) and (F) $Ni@CeZrO_2$.

Figure 19. Raman spectra of post-reaction catalysts.

Figure 20. DTG of the post-reaction samples.